CHEMISTRY OF MATERIALS

pubs.acs.org/cm Article

Factors Determining Microporous Material Stability in Water: The Curious Case of SAPO-37

Georgios N. Kalantzopoulos,* Fredrik Lundvall, Knut Thorshaug, Anna Lind, Ponniah Vajeeston, Iurii Dovgaliuk, Bjørnar Arstad,* David S. Wragg, and Helmer Fjellvåg

Cite This: *Chem. Mater.* 2020, 32, 1495−1505 Read Online

ACCESS | Metrics & More | Article Recommendations | Supporting Information

ABSTRACT: Silicoaluminophosphates (SAPOs) are a special class of zeolites that, due to their acidic and shape-selective properties, play a major role in ion exchange and separation processes and in crude oil cracking. SAPO-37 has the faujasite (FAU) topology same as zeolites X and Y, which are involved in more than 40% of the total crude oil conversion worldwide. A critical parameter that promotes detrimental structural transformations in SAPOs during real-life applications is the presence of humidity. In this study, we employ a multidisciplinary approach combining in situ synchrotron radiation powder X-ray diffraction (SR-PXRD), water adsorption, diffuse reflectance infrared Fourier transform spectroscopy (DRIFTS), and density functional theory (DFT) calculations to describe the mechanism and reveal the reasons why SAPO-37 collapses upon contact with humidity below 345 K. SR-PXRD revealed that the sodalite (SOD) cages (subunits of the FAU structure) have the strongest affinity to water during hydration below 345 K. Furthermore, below 345 K, the faujasite framework takes up an order of magnitude more water molecules than at temperatures above 345 K. DRIFTS confirmed the presence of Si−OH and P−OH surface structural defects that act as hydration centers, accelerating the loss of a long-range order. Finally, DFT calculations showed that the enthalpy of water adsorption in the sodalite cage and the faujasite supercage is −212 and −13 kJ/mol, respectively. The results presented in this work are highly topical for understanding the effect of water on the frameworks of the SAPO microporous catalysts family. The notorious instability of SAPO-37 is the result of the accumulative contribution of topological, physical, and chemical effects, leading to an array of rapidly evolving cascading effects. Our work shows how advancements in SR-PXRD methodology and hardware give new insight into highly dynamic features previously difficult to observe. In addition, this work introduces the conceptual insight that nonhomogeneous sorption of molecular species will induce dynamic features with dramatic consequences at both molecular and atomic levels. This is a highly impactful factor opening research paths for further work within catalysis, porous material design and chemistry, and sorption reactions and processes.

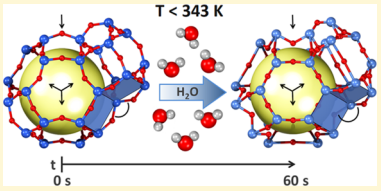

INTRODUCTION

Zeolites are used in catalytic, ion exchange, and separation processes in several industries, and due to their acidic and shape-selective properties, they play a major role in crude oil cracking.[1] The search for zeolite structures made with large pore windows for enhanced accessibility to their acid sites, led to the employment of the faujasite zeolites and variants of the material such as zeolites X, Y, and the ultrastable Y by a variety of industries. Today, more than 40% of total crude oil conversion takes place within the walls of a microporous catalyst with the faujasite structure.[2] Silicoaluminophosphates (SAPOs) are a special class of zeolites where a framework of tetrahedrally oxygen-coordinated Al and P has been partially substituted by Si creating a Brønsted acid site.[3] Due to its highly crystalline structure, large pore opening, and high surface area, SAPO-37 is a key material in processes such as the isomerization of *n*-decane,[4] isobutene/2-butene alkylation,[5] o-xylene isomerization,[6] or as a gas adsorbent.[7]

SAPO-37, has the same faujasite (FAU) topology as found in zeolites X, Y, and the ultrastable Y (USY). It is a highly crystalline microporous material possessing a 3D network where tetrahedrally coordinated T atoms (T = Al, P, or Si) compose sodalite cages (SOD) linked by double 6-rings (d6r: meaning two rings of 6 T-atoms). The 3D arrangement of the SOD cages form large 12-membered rings and create the faujasite supercage (FAU). We can describe the local T-atom environment as Si-substituted $AlPO_4$ tetrahedra (Si substituting P and/or Al) with Si, Al, and P being homogenously distributed around the framework.[8] The structure can also be visualized as a tetrahedral array of SOD cages interconnected by d6rs. This interconnected array of channels and cages forms the characteristic cubic structure of faujasite that crystallizes in the space group $Fd\bar{3}m$ with a typical cubic unit cell dimension of a = 24.345 Å for SAPO-37. The FAU supercage has an inner diameter of 11.2 Å where the 12-ring has a diameter of 7.4 Å (distance across diametrically opposite oxygen atoms), allowing molecules with

Received: November 1, 2019
Revised: January 21, 2020
Published: January 22, 2020

https://dx.doi.org/10.1021/acs.chemmater.9b04510
Chem. Mater. 2020, 32, 1495−1505

diameters of up to 7.3 Å to diffuse freely through the channels.[9] However, due to molecular vibration, molecules possessing critical diameters of up to 9.5 Å can also penetrate the faujasite porous network at moderate temperatures.[10]

SAPO-37 is synthesized with a dual-template method. Tetramethylammonium hydroxide (TMA) is used to form the SOD cages, and tetrapropylammonium hydroxide (TPA) is used for the assembly of the large FAU supercage.[11] Removal of these templates requires higher temperatures than usual when compared to other SAPO synthetic zeolites.[12] By itself, TMA combusts at a moderate temperature (473 K). In the case of SAPO-37, however, it is not until the FAU supercage is almost cleared of the TPA template that TMA can begin its combustion. This takes place between 690 and 945 K, inducing unusual local geometric responses to the thermal events.[12] During this procedure, the Brønsted acid sites are created, turning the material from a template-stabilized structure into a crystalline, catalyst framework.[8,11,12]

A critical parameter that promotes structural changes in SAPOs during real-life applications is the presence of humidity.[13,14] Water is an irreplaceable and frequently also an unavoidable component of real-life applications,[15] and its effect on the local structure of the framework needs to be carefully studied and understood. Although template-free SAPO-37 has exceptional hydrothermal stability at high temperatures (T > 1000 K), it has surprisingly poor stability below 345 K.[16] In 1987, Sierra de Saldarriaga et al. observed that exposure of template-free SAPO-37 to atmospheric humidity at temperatures close to RT induces a shrinkage of the unit cell.[8] Later, Briend et al. reported that the material begins contracting and loses crystallinity below 345 K at a rate that increases the closer the temperature is to RT.[16] To date, the mechanism behind this unforeseen crystallinity loss has not been experimentally revealed. One early suggestion for explaining the poor, low-temperature hydrothermal stability was that unfavorable P−O−P bonds would form during the template removal process. Yet, to date, all the NMR studies have unanimously shown only one type of phosphorus local environment in the as-calcined SAPO-37 framework: a phosphorus atom coordinated to four aluminum atoms (P(4Al))[8,11,16−18] as expected by charge balance considerations. In an attempt to systematically assess the hydrothermal stability of SAPO-37, Corma et al. observed at least six types of hydroxyl groups at 573 K that were formed during the template removal process.[17] Among these, terminal SiO−H and PO−H were detected and remained present up to the end limit of the applied heat treatment at 873 K. Out of the four other hydroxyl species two were considered to be bridging Si−OH−Al directed toward the supercage and to the sodalite cages, while two types of hydroxyls were associated with remaining organic templates. When the authors performed partial template removal at 673 K (removing the TPA^+ from the FAU supercage but keeping the majority of TMA^+ in the SOD cage), the material preserved its crystallinity in presence of atmospheric humidity for substantially longer time. They suggested that calcination at 873 K would favor the condensation of some Si−OH and P−OH species leading to formation of Si−O−Si and P−O−P bonds. The latter is highly susceptible to hydrolysis upon exposure to water at near ambient temperature. However, they made no direct experimental observation of P−O−P species. These observations will be discussed in light of our new data.

Although the loss of long-range order in SAPO-37 has been known since the first reports of the material, no data are reported on how hydration affects the specific surface area (SSA), pore volume, and mean pore diameter. Furthermore, the fine interplay between water and the SAPO-37 framework has never been elucidated. One hypothesis is that water adsorption dynamics should play a role,[16] but relevant experimental data is lacking. The reasons are partially due to the metastability of SAPO-37 in presence of water at temperatures below 345 K and partially due to lack of advances in the field of water adsorption assessment. The recent advances in minimizing the error propagation and significantly enhancing the reproducibility in sorption assessment by the Sieverts technique,[19] which stem from the boom in hydrogen storage research,[20] have now opened new opportunities for detailed insight.

Other SAPO frameworks such as SAPO-34, a key industrial catalyst in the methanol-to-olefin (MTO) conversion, are also affected by humidity at low temperatures, but the destabilization progresses at very slow rates.[21] SAPO-37, on the other hand, shows rapid and drastic loss in hydrothermal stability at low temperatures.[16] As a highly crystalline material[12] that does not form intergrowths like SAPO-34[22,23] but shares the same active chemistry,[18] SAPO-37 makes an excellent model material to study the effect of humidity on SAPO frameworks in general.

In this study, we present and discuss data on how water accumulates on the SAPO-37 surface and propose a mechanism of how the water concentration grows within the structure of the framework. High time- and space-resolution synchrotron radiation powder X-ray diffraction (SR-PXRD) reveals, for the first time, the local transformations connected with hydration in each of the SAPO-37 cage types. We evaluate the SAPO-37 water adsorption capacity above and below the critical temperature of 345 K while monitoring the changes in SSA, pore volume, pore size distribution, and crystallinity before and after each measurement. The presence of surface defects after calcination and the local interaction of water with the SAPO-37 framework during hydration were probed by diffuse reflectance infrared Fourier transform spectroscopy (DRIFTS). Density functional theory (DFT) calculations confirmed the preferential adsorption sites of water in the structure that were revealed by SR-PXRD. We also investigate the effect of SAPO-37 topology and of possible surface defects with respect to the material stability and critically discuss our results in view of the existing literature.

EXPERIMENTAL SECTION

Material Synthesis. SAPO-37 was synthesized according to literature procedures.[24] Details are provided in the Supporting Information.

In Situ Synchrotron Radiation Powder X-Ray Diffraction (SR-PXRD) Hydration. In situ SR-PXRD measurements were performed at the Swiss−Norwegian beamlines (station BM01)[25] at The European Synchrotron Facility (ESRF) in Grenoble, France. A fresh as-synthesized SAPO-37 sample was placed in a 0.5 mm quartz capillary and mounted in a flow cell that provides a controlled atmosphere. For calcination, the sample was heated up to 1073 K at 2 K min^{-1} in flowing synthetic air using a hot air blower. For hydration experiments, nitrogen was passed through a water-filled bubbler kept at ambient temperature. Temperature calibration was performed by measuring a sample of high purity Ag and Al_2O_3. The SR-PXRD patterns (exposure time 6 s) were collected using a Dectris Pilatus 2 M photon counting pixel area detector[25] and integrated with the SNBL Bubble software.[26] The wavelength, λ = 0.71210 Å was calibrated from individual runs with LaB_6.

Powder X-Ray Diffraction (PXRD). In-house powder X-ray diffraction (PXRD) data were recorded at ambient atmosphere and temperature on a Bruker D8-A25 instrument using monochromatic Cu

https://dx.doi.org/10.1021/acs.chemmater.9b04510
Chem. Mater. 2020, 32, 1495−1505

$K\alpha_1$ radiation (λ = 1.5406 Å) from a fine-focus sealed tube source and a LynxEye XE position-sensitive detector operated in transmission geometry.

X-Ray Diffraction Data Processing. The patterns were analyzed by parametric Rietveld refinement[27] using TOPAS[28] to extract the unit cell parameters, framework atom positions, isotropic thermal displacement parameters (B-iso) and water occupancy as a function of temperature. A single B-iso parameter was refined for all oxygen atoms. Diamond[29] and Vesta[30] were used for illustrating the crystal structures. Adobe Photoshop CS6 was used for the blending of the different time-frame illustrations in Figure S7.

Water and Nitrogen Adsorption Measurements. Nitrogen and water sorption measurements were performed on a BelSorp Max instrument at 77 K for nitrogen and at 353 and 323 K for water. Prior to each sorption measurement (nitrogen or water) annealing took place for 2 h at 423 K in a He atmosphere to remove any residual gas species from the porous material. All measurements and heat treatments took place sequentially to avoid any exposure of the samples to atmospheric air.

The measurement procedure to assess the hydration/water adsorption effect on template-free SAPO-37 was as follows.

$$\underset{77\ \mathrm{K}}{\overset{N_2\ \text{adsorption (SSA, PSD)}}{\longrightarrow}} \underset{353\ \mathrm{K}}{\overset{H_2O\ \text{adsorption (80 °C)}}{\longrightarrow}} \underset{77\ \mathrm{K}}{\overset{N_2\ \text{adsorption (SSA, PSD)}}{\longrightarrow}} \underset{323\ \mathrm{K}}{\overset{H_2O\ \text{adsorption (50 °C)}}{\longrightarrow}} \underset{77\ \mathrm{K}}{\overset{N_2\ \text{adsorption (SSA, PSD)}}{\longrightarrow}}$$

PXRD measurements took place before the first N_2 adsorption and after each subsequent N_2 adsorption measurement. Given the notorious instability of the material upon exposure to humidity, the transfer and loading times from the calcination oven to the sorption instrument or the XRD apparatus capillary were restricted to less than 30 min and under low relative humidity atmosphere (<50%). To avoid unnecessary exposure of the material to humidity between the two water adsorption measurements, two cells were run in parallel; cell 1 underwent the whole multistep experiment, whereas cell 2 was removed after the second nitrogen adsorption measurement for the assessment of the structural degradation via PXRD. The timeline evolution of this multistep experiment is provided in the Supporting Information (Figure S8).

The total SSA was extracted from the nitrogen adsorption isotherms via the Brunauer–Emmett–Teller (BET) method according to the literature.[31] Nonlocal density functional theory (NLDFT) calculations of the pore size distribution (PSD) were performed using the commercial BELMaster software from MicrotraBEL Corp. The NLDFT calculation method was applied on the adsorption branch using the N_2 physisorption data collected at 77 K. For the calculations, a cylindrical pores model was assumed.

The evaluation of the number of H_2O molecules per surface unit took place using eq 1, where N_A is the Avogadro number, wt % is the gravimetric adsorption, MW_{gas} is the molecular weight of the adsorbed fluid, and SSA is the specific surface area obtained by BET.[32−36] The values of the SAPO-37 occupiable[i] and accessible[ii] surface areas were obtained by the literature.[37]

$$\frac{N_{molec}}{nm^2} = \frac{N_A \times \mathrm{wt\%}}{10^{20} \times MW_{gas} \times SSA} \quad (1)$$

In order to gain a deeper insight into adsorbant–adsorbent interaction, the experimentally obtained data were fitted according to the Tóth model[38] (eq 2), where wt $\%_{max}$ is the asymptotic maximum storage capacity, K is the equilibrium constant, P is the pressure, and t is a parameter introduced by Tóth in order to describe the level of homogeneity of the sample surface.

$$\mathrm{wt\%} = \mathrm{wt\%}_{max} \frac{KP}{(1 + (KP)^t)^{1/t}} \quad (2)$$

Diffuse Reflectance Infrared Fourier Transform Spectroscopy (DRIFTS). We performed DRIFTS measurements on template-free SAPO-37 under similar conditions as the in situ SR-PXRD and the water adsorption measurements. The experimental details and spectra can be found in the Supporting Information.

Computational Details. Quantum-mechanical calculations via the density functional theory (DFT) method were performed on the template-free SAPO-37 framework. The computational details and main results can be found in the Supporting Information.

RESULTS

In Situ SR-PXRD Hydration. Recently, we studied the template removal of SAPO-37 in situ, revealing the subunit cell transformations that take place in the framework during

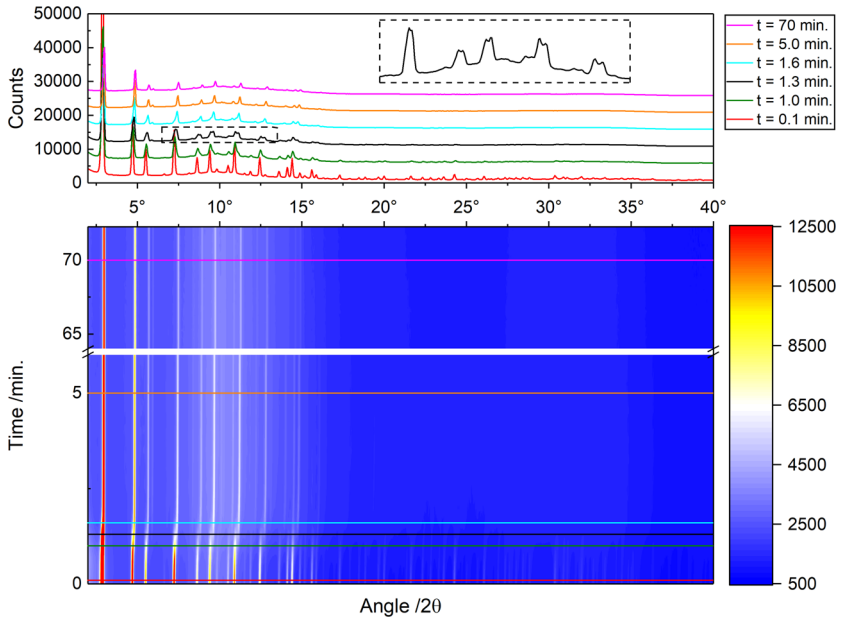

Figure 1. 2D film plots of the evolution of the template-free SAPO-37 diffraction patterns during the first hydration period at 313 K (λ = 0.71210 Å). Selected diffraction patterns highlighting critical differences between the dry and hydrated material are shown in the top panel. The colored horizontal lines on the 2D film plot (bottom) indicate the time stamp for each of the selected diffraction patterns (top) by following the same color coding. The coexistence of the wet and hydrated SAPO-37 phases is illustrated in the dashed inset.

https://dx.doi.org/10.1021/acs.chemmater.9b04510
Chem. Mater. 2020, 32, 1495−1505

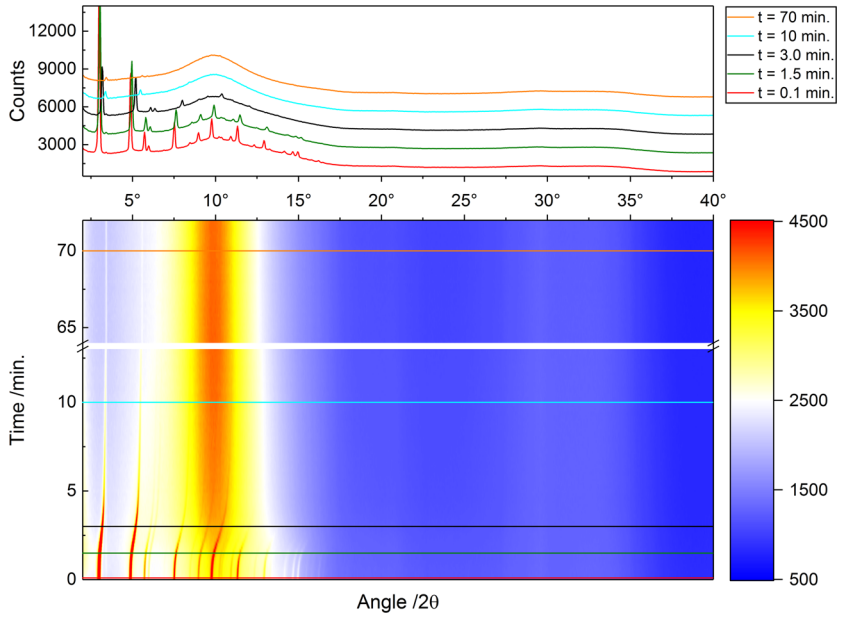

Figure 2. 2D film plots of the evolution of the template-free SAPO-37 diffraction patterns during the second hydration period in the temperature range 313−473 K. Selected diffraction patterns illustrating the evolution at critical time frames are shown in the top panel. The colored horizontal lines on the 2D film plot (bottom) indicate the time stamp for each of the selected diffraction patterns (top) by following the same color coding. The wavelength is λ = 0.71210 Å.

calcination, resulting in a highly crystalline material.[12] Building on the template removal study, we exposed the same powder sample to a variety of atmospheres at a low (313 K) temperature. From these experiments we evaluated the low temperature stability of SAPO-37 in argon, atmospheric air (40−50% relative humidity), and in water-saturated Ar, under constant (313 K) and variable temperature conditions. A schematic timeline summarizing all the different experimental conditions is presented in the Supporting Information (Figure S2).

In the first part of the experiment, the template-free material was exposed to inert atmosphere (100% Ar) at 313 K for 190 min. In those conditions, no changes can be detected in the diffraction patterns (Figure S3). The structure is stable and retains its crystallinity over time. Then, we switched to atmospheric air (40−50% relative humidity at 313 K) for about 100 min. In those conditions, the diffraction patterns look macroscopically unchanged (Figure S4, top). However, a closer analysis reveals that after a short induction period, the SAPO-37 framework undergoes a small unit cell volume loss that progresses at the rate of 1 Å^3/min (Figure S4, bottom). It is interesting to note that despite the absence of easily visible changes in the diffraction patterns, the degree of crystallinity (DoC) is profoundly affected. The DoC was calculated comparing the relative area of the strongest reflections (111 and 222) in each pattern with their corresponding area in the diffraction pattern of the fresh, template-free material according to eq 3.

$$\text{degree of crystallinity, DoC} = \frac{\text{area}_{hkl_{\text{peak},i}}}{\text{area}_{hkl_{\text{peak},0}}} \times 100\% \quad (3)$$

where hkl = 111 and 222 of PXRD pattern i of the hydrated material, compared to hkl = 111 and 222 of the starting PXRD pattern o obtained from the completely dry, template-free framework.

In the next step, the material is exposed to water-saturated Ar for about 70 min at the same temperature (313 K). In those conditions, template-free SAPO-37 undergoes a plethora of subunit cell structural transformations in a short amount of time. At the beginning of this hydration period at 313 K, the DoC of SAPO-37 is virtually unchanged (99 and 94% for the (111) and (222) reflection, respectively, Figure S5) compared to the freshly calcined material. The diffraction peaks are well-resolved up to very high angles (d spacing < 1 Å, Figure 1, top). Within the first 30 s of the experiment, the diffraction pattern remains unchanged, probably due to the dead volume in the gas system. After these first seconds, there is a rapid change to all main reflections (2θ = 4.0−15.5°), corresponding to d spacing 8.7−2.6 Å, as they are shifted toward higher 2θ values. The changes are clearly visible in the diffraction patterns of the top panel of Figure 1. In the diffraction pattern recorded at 1.3 min, the coexisting dry and hydrated phases are visible as peak splitting in several of the low-angle (e.g., 331, 511, 044, and 533 reflections, Figure 1 top, dashed inset) reflections. As the hydration proceeds, we observe a substantial loss of peak intensity, clear peak broadening, and a noticeable increase in the background level. After 90 s, the reflections corresponding to d spacing ≤ 2.5 Å are all lost. Interestingly, this d spacing coincides with the kinetic diameter of water (2.65 Å). At the same time, the 822 and 555 reflections (d spacing = 2.83 and 2.77 Å) show a severe splitting that appears with a small delay compared to the lower 2θ reflections. This behavior is interpreted as a delayed response to the diffusion of water molecules into a tight, confined space. After 120 s of hydration, the nonhydrated phase cannot be detected anymore, and practically all the reflections with d < 2.75 Å have disappeared. It is important to note that the loss of high-angle reflections does not necessarily imply at this point a total loss of long-range order and structural collapse, but rather a local disorder caused by water on a subunit cell level. The high-angle reflections of the material are effectively masked by the incoherent scattering of water even if the structure is in fact still present.

In the last part of the experiment, the temperature was increased from 313 to 473 K at 5 K min^{-1} while maintaining the

https://dx.doi.org/10.1021/acs.chemmater.9b04510
Chem. Mater. 2020, 32, 1495−1505

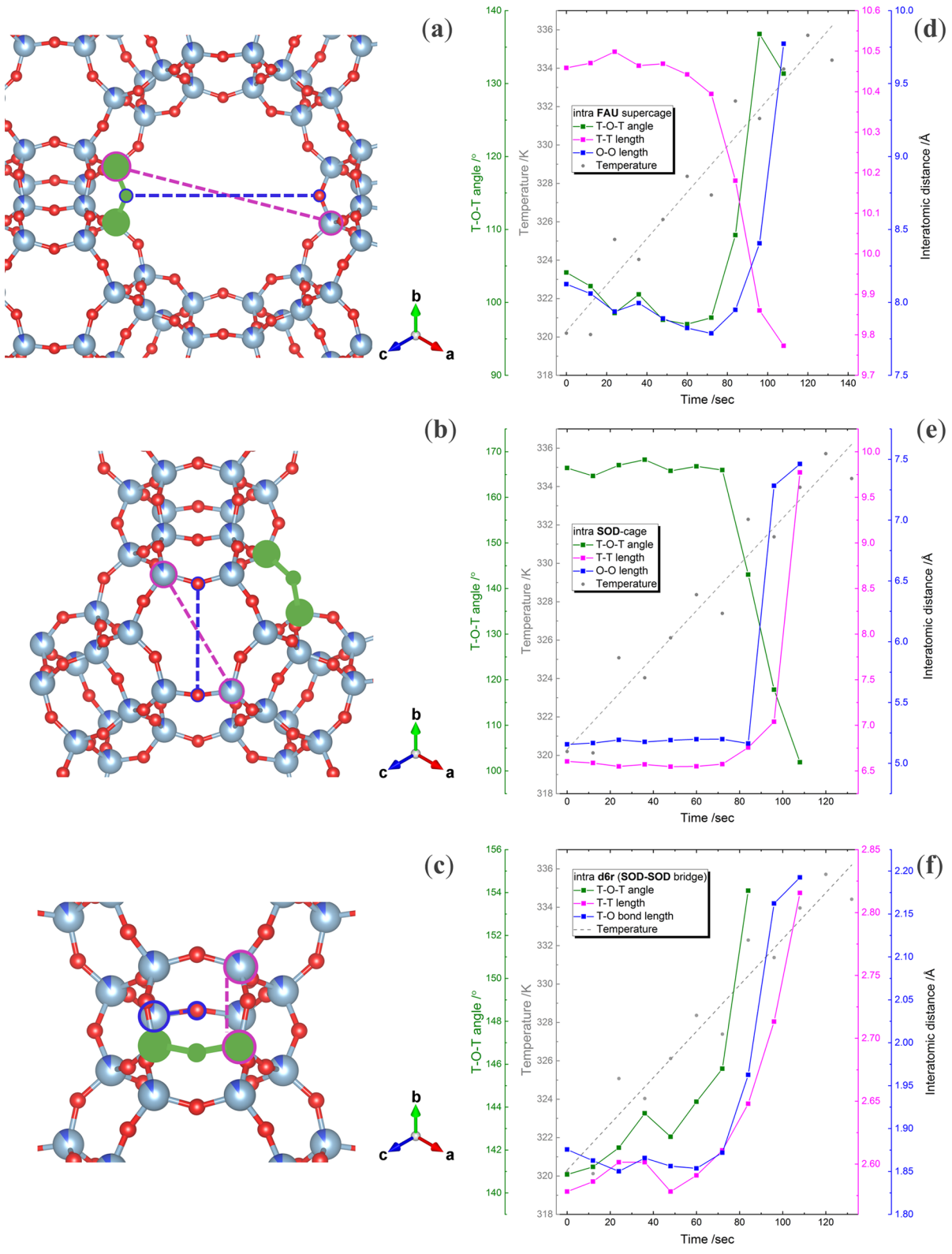

Figure 3. Variation of selected T−O−T angles, T−T, and O−O distances for (a) the FAU supercages, (b) the SOD cages, and (c) the d6r bridging units Selected T−O−T angles, T−T, and O−O distances for (a) the FAU supercage, (b) the SOD cage, and (c) the d6r bridging units. The variation of the selected T−O−T angles, T−T, and O−O distances are illustrated in panels (d)−(f) for the FAU supercage, the SOD cage, and the d6r bridging units, respectively. The estimated standard deviations are below 0.015 Å for the distances and 0.4° for the angles (T-atom: blue, O-atom: red).

hydration feed (Figure 2). During the first 1.5 min (T = 313−323 K), there is a peak intensity loss and a shift of the reflections toward higher values. After 1.5 min (T = 323−333 K) the changes become more rapid and pronounced, as the hydrated material responds to heating. This transition over the first 3 min is accompanied by a dramatic loss in peak intensity. Furthermore, the loss of peak intensity is strongly correlated with an increase in the background in the 2θ = 6−15° range,

https://dx.doi.org/10.1021/acs.chemmater.9b04510
Chem. Mater. 2020, 32, 1495−1505

indicating the gradual formation of a poorly ordered phase. Further increase in temperature leaves only the first two reflections (111 and 022) visible.

For this section of the experiment, it was possible to follow the transition via parametric Rietveld refinement for the first 4.25 min, up to 353 K (vide infra). Above this temperature, we could only monitor the structural degradation via parametric peak fitting of the 111 and 022 reflections. The DoC and unit cell volume loss (assuming that the SAPO-37 unit cell is still present) are shown in Figure S6. Another interesting observation made in those conditions is that the (111) degree of crystallinity is affected more strongly than the (222) degree of crystallinity (Δ_{111}^{DoC} = 46.1 % vs Δ_{222}^{DoC} = 32.4%) pointing toward a rupture of the FAU supercages and consecutive loss of the long-range order.

From the crystallinity and cell volume variation versus time plots, it is easily noticeable that crystallinity loss and change in the cell volume are two independent phenomena since different diffraction peaks have different DoC loss profiles. In essence, a reflection corresponding to a small *d* spacing will have a different response to inclusion, adsorption, or accumulation of water molecules compared to a reflection from a larger *d* spacing that would be influenced by the accumulative effect of water in different subunit cell regions. Large cages would have slower response to water accumulation compared to the narrower parts of the unit cell, such as the SOD cages or the d6rs.

In order to describe the geometric response of different domains of the SAPO-37 unit cell during the first seconds of hydration under heating (Figure 2), we have plotted selected T−O−T angles, T−T, and O−O distances for the FAU supercages, the SOD cage, and the d6r bridging units (Figure 3). As a typical T−O−T angle in the FAU supercage, we selected a T−O−T linkage in the d6r with the oxygen atom pointing toward the supercage (Figure 3a). Rather than monitoring the bond length of a given T−O pair, we followed the variation of the FAU supercage opening diameter (12-ring) using the distance of two diametrically opposite T−T and O−O pairs (dashed blue lines in Figure 3a). In the SOD cage, we selected a T−O−T linkage shared between the FAU supercage and the SOD cages (Figure 3b). As representative T−T and O-O distances of the SOD cage, we selected T- and O-atoms belonging to the 6-ring interface between SOD and FAU supercages for monitoring. In the d6r bridging units, we monitored a T−O−T linkage (green) shared between the 4-ring of the SOD cage and the d6r unit, a T−T pair representing the distance between the two SOD cages (dashed blue line and along the d6r), and finally an individual T−O bond length of the same entity used in the T−O−T angle (Figure 3c). For the latter, an equivalent position is shown in blue on Figure 3c for the sake of clarity.

During the first 60 s of heating in humid Ar from 313−473 K at 10 K min^{-1} there is practically no structural response to the heating, probably due to a delayed thermal response in the experimental setup. After this initial delay, there are considerable and rapid changes occurring in each individual domain of the unit cell. In the FAU supercage, the T−O−T angle increases substantially from 95 to 132° in less than 45 s (Figure 3d). Simultaneously, the T−T and O−O distances have completely opposite individual responses. The T−T distance decreases from 10.4 to 9.75 Å, whereas the neighboring O−O distance shows a substantial increase from 7.7 to 9.7 Å, which effectively is a consequence of widening of the aforementioned T−O−T angle. In the SOD cage, the monitored T−O−T angle decreases from 166 to 101° in a matter of 40 s. At the same time, both the T−T and O−O distances increase substantially from 6.60 to 9.77 Å (48% extension) and from 5.15 to 7.46 Å (45% extension), respectively (Figure 3e). Finally, in Figure 3f, we see that there is a substantial expansion within the d6r and particularly in the SOD−d6r interface until reaching the breaking point (on selected T−O−T bonds). This T−O−T angle is the first part of SAPO-37 to respond to the increasing temperature during hydration, becoming wider already 20 s within the experiment. Overall, the T−O−T angle widens from 140 to 154° (Figure 3f). Simultaneously, the T−T distance between two SOD cages increases from 2.57 to 2.82 Å (9.7% extension) and has a similarly fast response as the T−O−T angle (Figure 3f). The T−O length increases from 1.87 to 2.19 Å (Figure 3f). The starting value (1.87 Å) is already 15% longer than the nominal T−O of the template-free SAPO-37 (average T−O length in our sample at RT, 1.625 Å). As the hydration continues and the temperature increases, this length reaches a value that is 17% higher with respect to the beginning of the experiment (and 35% with respect to the average T−O length of the dry, template-free framework). This is the largest bond length variation found in the framework during this experiment. As such, it is a clear indication that this point in the framework is critical during the structural collapse.

From the above analysis, we can observe that each building unit has a slightly different time response to the temperature change during hydration. The smallest volume (d6r), responds to heating first, followed by a contraction of the large FAU supercage and the distortion of the SOD cage. This can be explained if we assume that water is primarily concentrated in the SOD cage and in the SOD−d6r interface. Note that the structural changes in the FAU supercage are primarily due to the geometric responses occurring to each of the six surrounding SOD cages and the d6rs. A graphical illustration comparing the dry and hydrated framework at selected time-frames up to the point of the selected T−O bond failure is shown and discussed in detail in Figure S7.

Water Adsorption on SAPO-37. In order to further understand water's role in the destabilization of the SAPO-37 framework, we performed water adsorption measurements above and below the critical temperature of 345 K. Measurements were carried out first at 353 K and subsequently at 323 K where the interaction of water with the framework is anticipated to be very strong. Specific surface area and crystallinity were assessed by nitrogen physisorption measurements and PXRD at defined stages throughout the experiment, as described in the Supporting Information (Figure S8).

At 2.75 kPa, the material surface retains 7.1 H_2O molecules per unit cell, corresponding to a surface density of 0.31 H_2O molecules per nm^2 in both sample cells (Figure 4). By comparison, water adsorption on SAPO-37 at 323 K shows a multistep surface-filling mechanism (Figure 4). During the very first adsorption steps ($p < 0.05$ kPa), the material uptakes 5.0 H_2O molecules per unit cell, which is comparable to the total capacity at 353 K and 2.75 kPa. As the pressure increases, the adsorption continues linearly until a second adsorption step is seen in the pressure region 0.2−0.5 kPa. A small shoulder can be observed at 1 kPa before the adsorption capacity reaches a quasi-saturation plateau. Above that pressure, the adsorption continues linearly and at a substantially lower rate (3.8 H_2O molecules per kPa). Compared to the isotherm at 353 K, the number of H_2O molecules per unit cell at 323 K is an order of magnitude higher, and the H_2O molecules per surface unit increases by a factor of seven (Figure 4).

https://dx.doi.org/10.1021/acs.chemmater.9b04510
Chem. Mater. 2020, 32, 1495−1505

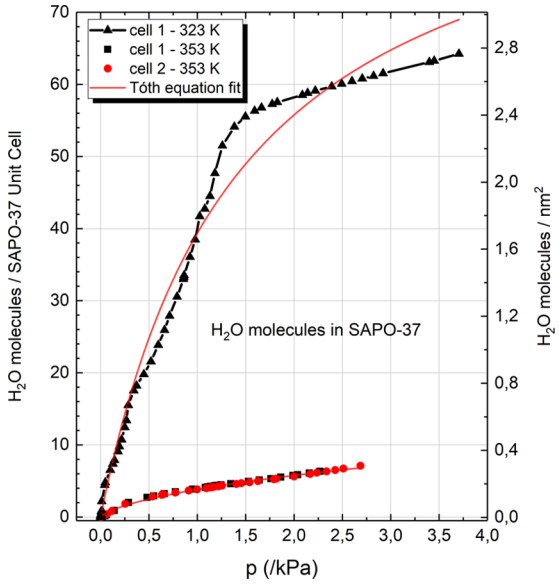

Figure 4. Number of H_2O molecules per SAPO-37 unit cell and H_2O molecules concentration per surface area unit during H_2O adsorption at 353 and 323 K. The isotherms are fitted with the Tóth model. The purpose of running two parallel sample cells (cells 1 and 2) is illustrated in Figure S8 in the Supporting Information.

In order to obtain more quantitative information, the isotherms were fitted with the Tóth model (eq 2). The model was selected due to its ability to describe the adsorbant coverage over a variety of adsorbent surfaces and porous structures[34,36] and complex hybrid materials that offer a variety of adsorption sites within the same framework.[35] The water adsorption isotherm at 353 K shows a multistep adsorption mechanism with a total uptake of 33 wt % (Figure S9, Supporting Information) corresponding to 64 H_2O molecules per unit cell (Figure 4). According to the Tóth model fitting, the surface has a theoretical capacity of 95 H_2O molecules per unit cell at these pressure and temperature conditions. Note that the multistep adsorption leads to a comparatively poor fit of the Tóth model and the maximum theoretical capacity should be regarded as a rough estimation that will not be discussed further. Details in the results are reported in Table S1.

Diffuse Reflectance Infrared Fourier Transform Spectroscopy (DRIFTS). To obtain complementary data to PXRD, when SAPO-37 interacts with water, we performed DRIFTS measurements, and the overall interpretation and analyses of these data are in agreement with our in situ SR-PXRD and the ex situ structural analysis of the samples after water adsorption. After the in situ calcination of the as-synthesized material under synthetic air in the DRIFTS sample cell, the spectrum shows all the key features reported by Corma et al.[17] (Figure S13a in the Supporting Information). Band assignment can be found in the Supporting Information.

The band positions observed in template-free SAPO-37 and after annealing at 423 K are the same, but their intensities are somewhat lower in the latter. This suggests that 423 K is a sufficient temperature for dehydration of the framework, although there are some minor irreversible material changes likely due to interaction with water. After exposure to H_2O at 323 K (Figure S13d), the bands assigned to −OH groups in the sodalite cage and supercage are barely observed in the spectra, suggesting that the cages have collapsed. Heating to 423 K and then to 723 K does not regenerate the SAPO-37 (Figure S13e). The main bands observed in the final material coincide with the bands assigned to P−OH and Si−OH in template-free SAPO-37. From spectra (Figure S13), we infer that the structure deterioration is more pronounced at 323 K than at 353 K due to the less-resolved bands.

Quantum-Mechanical Calculations via the Density Functional Theory (DFT) Method. We performed DFT calculations on template-free SAPO-37 framework in order to assess the effect of topology and local geometry on the enthalpy of water adsorption and to identify the areas within the SAPO-37 framework with highest affinity to water. The computational details and more detailed results can be found in the Supporting Information.

According to the calculations, the H_2O adsorption energy value for the SOD cage site and the FAU supercage site are −212 and − 13 kJ/mol respectively. This difference in magnitude of the adsorption energy clearly indicates that the H_2O absorption in SOD cage is much more energetically favorable than in the FAU supercage.

Figure 5 shows the calculated water density in the SAPO-37 framework and in SOD cages. The water density in the SOD

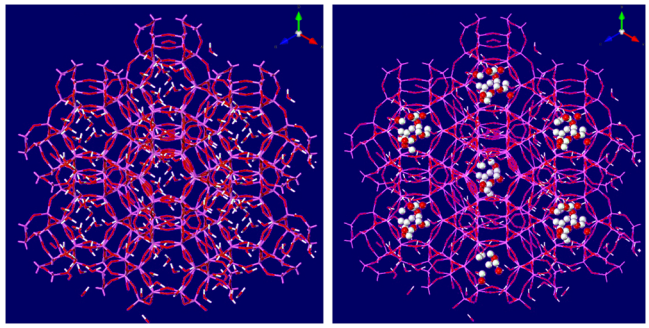

Figure 5. Water molecules embedded into the whole SAPO-37 framework as viewed along the 111 direction (left). Spheres highlight the water concentrated only in the SOD cages (right).

cages is clearly higher compared to the water density in the FAU supercage environment. Interestingly, the water molecules in the FAU supercages have higher concentration along the channels interconnecting the FAU supercages. The calculated distribution of the H_2O−H_2O molecule distance in the material is shown in Figure S14. The largest fraction of water molecule pairs has a calculated average distance that is less than 1.8 Å, indicating a medium-strength H-bonding.[39] Most of them (>60%) were found to be concentrated in the SOD cage (Figure S14, top).

DISCUSSION

Structural Transformations Induced on the SAPO-37 Framework during Low-Temperature Hydration. Our results indicate that as the dry and template-free SAPO-37 is being hydrated, water molecules accumulate within the narrowest internal domains of the framework, namely the SOD cages and the d6r units. The Brønsted acidic centers (one per SOD cage and 1.7 per FAU supercage on average) and the P−OH and Si−OH moieties (which are known to increase the hydrophilicity of the surface[40]) can act as local anchors for water molecules to the framework, enhancing the adsorbent/adsorbate interaction. The material has a pronounced water adsorption capacity, which is much greater at 323 K than at 353 K (observed by H_2O adsorption and corroborated by DFT

https://dx.doi.org/10.1021/acs.chemmater.9b04510
Chem. Mater. 2020, 32, 1495−1505

calculations). This suggests that at low temperatures, there is a significantly increased chance for water to be in close contact with the surface in the SOD cage or the d6r. At high loadings, the properties of this surface water layer approach those of bulk water. The high concentration of water around the acid centers and defects, combined with the confining geometry of the framework, result in the structural destabilization of the SAPO-37 framework. Adding thermal energy to a highly hydrated SAPO-37 accelerates the breakdown of the material.

The geometrical characteristics of the SOD−d6r−SOD interface provide an explanation as to why the structure ruptures at the T−O2−T moiety. This interface includes three adjacent 4-rings (Figure 6) where the T−O4−T angle is particularly

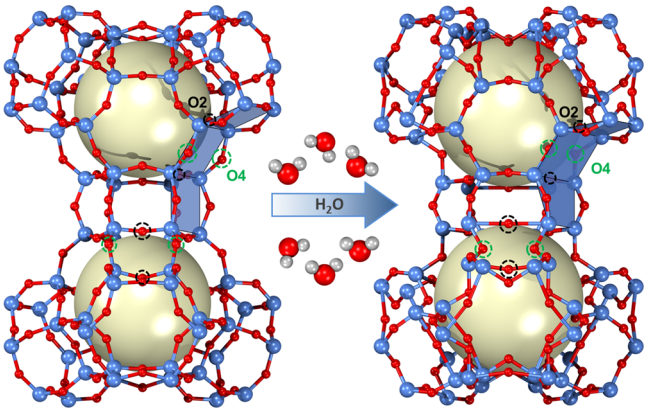

Figure 6. Excerpt of a completely dry, template-free SAPO-37 structure (left) and heavily hydrated SAPO-37 structure (right) highlighting the SOD−d6r−SOD interface. Selected O2- and O4-atoms are marked with black and green dashed circles, respectively. A triplet of adjacent 4-rings (4r) is indicated with blue planes. The internal volume of the SOD cages are indicated with yellow spheres (T-atom: blue, O-atom: red).

strained in the hydrated form of the material, compared with the dry template-free structure (166° vs 144° dry, O4: red spheres marked with green dashed circles in Figure 6). As the SOD cages distort during heating and hydration due to the massive uptake of water, increased pressure is applied to this area of the framework, observed as the dramatic change in the T−O4−T angle from 166 to 101° in a matter of seconds before the structure collapses. To accommodate this change in angle, the T−O2 bond of the strained 4-ring stretches from 1.87 to 2.19 Å in a concerted motion before it finally breaks (O2: red spheres marked with black dashed lines in Figure 6).

Mechanism of Water Attack on SAPO-37. Three earlier studies on zeolite stability in the presence of water show results that help us to understand our data. These studies have been mainly undertaken in the context of dealumination, but also include reactions with liquid water (important for biomass conversion using zeolites). Agostini et al. presented in situ XAS and PXRD data on the dealumination of zeolite Y.[41] They found that dealumination mainly takes place at 450−500 K, and that the efficiency of the process was low at 873 K, in contrast to previous common assumptions. Only minor structural changes occur in the presence of moisture at high temperatures.

Ravenelle et al. studied the reaction of several Y and ZSM-5 zeolites with hot liquid water at 423 and 473 K in autoclaves.[42] The stability depended strongly on the framework type, but for Y zeolite with Si/Al > 14, they found hydrolysis of Si−O−Si bonds at these relatively low temperatures.

Working at even lower temperatures, Heard et al. demonstrated the room temperature lability of zeolite CHA toward water using ^{17}O NMR.[43] They found that liquid water in the pores exchanged O-atoms with the framework at room temperature in less than 1 h. The authors furthermore presented a plausible novel reaction mechanism explaining their findings based upon ab initio molecular dynamics. Their mechanism is based on the Grotthuss mechanism with a proton shuttling over four water molecules. This mechanism is entropically demanding, and the reaction rates decrease with increasing temperatures. Other works have reported that CHA framework with Si/Al < 5, are highly susceptible to destabilization in an acidic environment.[44]

Based on our experiments, we propose a mechanism for how water accumulates and attacks the SAPO-37 framework resulting in its rapid, complete disruption. Water behaves quite differently in the relatively large FAU supercage compared to the more confined SOD cage and the d6r. The surface of the FAU cage has a smaller curvature than the SOD cage as well as a lower concentration (approximately half) of acidic centers per nm^2. As the template-free framework is exposed to water molecules, some will interact weakly with the surface of the FAU supercage. Others will enter the more confined and acidic SOD cage and d6r. Once a water molecule finds itself within the SOD cage or d6r, it is highly likely to get "trapped" there because of the local environment. This is strongly supported by our calculations, which show that ΔH_{ads} in this part of the framework is higher by a factor of 16 than in the FAU supercages.

From our experiments and calculations, it is clear that water accumulates initially in the small confined spaces in the SOD cages and the d6rs. This water space-filling procedure takes place rapidly and with significant consequences. In the confined environment of an SOD cage or d6r entity, the tightly packed cluster of water molecules is rather stable and should be able to deprotonate the corresponding acidic sites. It has been shown that clusters larger than 2−3 water molecules are able to deprotonate a zeolitic Brønsted site.[45,46] Alternatively, a mechanism similar to the one presented by Heard et al. might take place. Independent of the reaction, a highly acidic solution is localized in the SOD/d6r domain.[43] This is further supported by the fact that the SAPO-34 framework dissolves in 1 M HCl acid within minutes.[47] The change in the local pH could easily and quickly introduce local defects that will destabilize the framework, leading eventually to the loss of long range order by, for example, attacking and destabilizing the Al−O−P bonds. In contrast, the FAU supercages are far too large to form water clusters with the size and stability to initiate chemical attack in the framework and consecutive destabilization in a rate faster than that, which occurs in the SOD and d6r domains.

To conclude, it is tempting to speculate that there might be a common set of similar reaction mechanisms taking place when the zeolite pores are filled with water since higher temperatures strongly decrease the reactivities of the framework (in all situations, both for dealumination and Si−O−Si bond hydrolysis). The suggestion by Heard et al.[43] of an entropically demanding situation is reasonable. High temperatures and low coverage, together with faster transport and repositioning of water, hamper the reaction between water molecules and the framework.

CONCLUSIONS

We have performed a comprehensive multitechnique study on the effect of hydration on the SAPO-37 framework and

https://dx.doi.org/10.1021/acs.chemmater.9b04510
Chem. Mater. 2020, 32, 1495−1505

investigated the role that material topology and surface properties play on the material destabilization. In particular, we have followed the hydration of the framework with high time and space-resolution in situ SR-PXRD at constant and dynamic temperature conditions up to the point of multiple bond ruptures in the unit cell. Our work shows how advancements in XRD instrumentation can provide data of exceptionally high quality with excellent time resolution. Detailed analysis of the large datasets obtained from experiments of this type can furthermore be analyzed using methods such as parametric Rietveld refinement to give new insight to highly dynamic and subtle features previously difficult to observe or measure. In addition, we have measured water adsorption and collected DRIFTS spectra above and below the critical temperature of 345 K, the threshold temperature below which the framework substantially degrades. Finally, DFT calculations have provided a valuable support to the extensive experimental study.

The notorious instability of SAPO-37 can be explained as the cumulative contribution of topological, physical, and chemical events, leading to an array of rapidly evolving cascading effects. The narrow spaces in the SOD and d6r will physically trap water molecules. This preferred accumulation of water increases the mechanical strain, leading to the rupture of the d6r which were found to be the weakest structural element of the framework. As the water concentration increases, bulk-like water starts forming locally. When it gets in contact with the Brønsted acidic sites, it forms the highly acidic H_3O^+, which autocatalyzes the destruction of the SAPO framework.

We introduce the conceptual insight that nonhomogeneous sorption of molecular species will induce dynamic features with dramatic consequences at molecular and atomic levels, which is very important for further works. We expect that the methods used and the mechanisms found for SAPO-37 will be more broadly applicable in other framework materials. This work also provides a solid framework for advancing the models for gas−solid reactions.

■ ASSOCIATED CONTENT

Supporting Information

The Supporting Information is available free of charge at https://pubs.acs.org/doi/10.1021/acs.chemmater.9b04510.

Details on methods and protocols (both computational and experimental), including material preparation, film plots and figures based on PXRD data, further details on the water adsorption measurements, and IR and DFT results (PDF)

■ AUTHOR INFORMATION

Corresponding Authors

Georgios N. Kalantzopoulos − *Centre for Materials Science and Nanotechnology (SMN), Department of Chemistry, University of Oslo, Oslo N-0371, Norway;* orcid.org/0000-0001-9213-9752; Email: georgios.kalantzopoulos@kjemi.uio.no

Bjørnar Arstad − *SINTEF Industry, Oslo N-0373, Norway;* orcid.org/0000-0003-0398-786X; Email: bjornar.arstad@sintef.no

Authors

Fredrik Lundvall − *Centre for Materials Science and Nanotechnology (SMN), Department of Chemistry, University of Oslo, Oslo N-0371, Norway*

Knut Thorshaug − *SINTEF Industry, Oslo N-0373, Norway*

Anna Lind − *SINTEF Industry, Oslo N-0373, Norway*

Ponniah Vajeeston − *Centre for Materials Science and Nanotechnology (SMN), Department of Chemistry, University of Oslo, Oslo N-0371, Norway*

Iurii Dovgaliuk − *Swiss-Norwegian Beamline at the European Synchrotron Facility, Grenoble F-38000, France; Département de Chimie, ENS-UMR 8004 CNRS-ENS-ESPCI, Institut des Matériaux Poreux de Paris, Paris 75005, France;* orcid.org/0000-0003-1997-4748

David S. Wragg − *Centre for Materials Science and Nanotechnology (SMN), Department of Chemistry, University of Oslo, Oslo N-0371, Norway;* orcid.org/0000-0001-8502-7912

Helmer Fjellvåg − *Centre for Materials Science and Nanotechnology (SMN), Department of Chemistry, University of Oslo, Oslo N-0371, Norway*

Complete contact information is available at: https://pubs.acs.org/10.1021/acs.chemmater.9b04510

Notes

The authors declare no competing financial interest.

■ ACKNOWLEDGMENTS

The research leading to these results was funded by the project "Catlife: Catalyst transformation and lifetimes by in-situ techniques and modelling", P#233848" of the Research Council of Norway. Partial support was received by the Department of Chemistry at UiO and by the Interreg project MAX4ESSFUN−UiO-007 (project#190980) of the Research Council of Norway. We acknowledge the use of the Norwegian centre for X-ray diffraction and scattering (RECX, NFR project number 208896). P.V. acknowledges the Research Council of Norway for providing the computer time (under the project number NN2875k) at the Norwegian supercomputer. The authors thank the project team at BM01 from the Swiss-Norwegian Beamlines at the ESRF, France for their skillful assistance.

■ ADDITIONAL NOTES

[i]Area that can be occupied by a water molecule assuming a radius of 1.4 Å.

[ii]The continuous area that can be accessed by a water molecule, excluding pores/cavities too small to host a water molecule.

■ REFERENCES

(1) Weckhuysen, B. M.; Yu, J. Recent advances in zeolite chemistry and catalysis. *Chem. Soc. Rev.* **2015**, *44*, 7022−7024.

(2) Martino, G. Catalysis for oil refining and petrochemistry, recent developments and future trends. *Stud. Surf. Sci. Catal.* **2000**, *130*, 83−103.

(3) Lok, B. M.; Messina, C. A.; Patton, R. L.; Gajek, R. T.; Cannan, T. R.; Flanigen, E. M. Silicoaluminophosphate molecular sieves: another new class of microporous crystalline inorganic solids. *J. Am. Chem. Soc.* **1984**, *106*, 6092−6093.

(4) Mostad, H. B.; Stöcker, M.; Karlsson, A.; Rørvik, T. Comparison of the iso-structural H-SAPO-37 and H-faujasite as catalysts for the isobutane/2-butene alkylation. *App. Catal., A* **1996**, *144*, 305−317.

(5) Smith, L.; Cheetham, A. K.; Marchese, L.; Thomas, J. M.; Wright, P. A.; Chen, J.; Gianotti, E. A quantitative description of the active sites in the dehydrated acid catalyst HSAPO-34 for the conversion of methanol to olefins. *Catal. Lett.* **1996**, *41*, 13−16.

(6) Ojo, A. F.; Dwyer, J.; Dewing, J.; Karim, K. Synthesis and properties of SAPO-37. *J. Chem. Soc., Faraday Trans.* **1991**, *87*, 2679−2684.

(7) Verboekend, D.; Nuttens, N.; Locus, R.; Van Aelst, J.; Verolme, P.; Groen, J. C.; Pérez-Ramírez, J.; Sels, B. F. Synthesis, characterisation, and catalytic evaluation of hierarchical faujasite zeolites: milestones, challenges, and future directions. *Chem. Soc. Rev.* **2016**, *45*, 3331−3352.
(8) Sierra de Saldarriaga, L.; Saldarriaga, C.; Davis, M. E. Investigations into the nature of a silicoaluminophosphate with the faujasite structure. *J. Am. Chem. Soc.* **1987**, *109*, 2686−2691.
(9) Baerlocher, C.; McCusker, L. B. *Database of Zeolite Structures*, http://www.iza-structure.org/databases/ , (Accessed: Mar 15, 2019).
(10) Kärger, J.; Ruthven, D. M.; Theodorou, D. N. Large Pore (12-Ring) Zeolites. In *Diffusion in Nanoporous Materials*; Wiley-VCH Verlag GmbH & Co. KGaA, 2012; pp 607−651.
(11) Briend, M.; Lamy, A.; Peltre, M.-J.; Man, P. P.; Barthomeuf, D. Thermal stability of tetrapropylammonium (TPA) and tetra methylammonium (TMA) cations occluded in SAPO-37 molecular sieves. *Zeolites* **1993**, *13*, 201−211.
(12) Kalantzopoulos, G. N.; Lundvall, F.; Lind, A.; Arstad, B.; Chernyshov, D.; Fjellvåg, H.; Wragg, D. S. SAPO-37 microporous catalysts: revealing the structural transformations during template removal. *Catal., Struct. React.* **2017**, *3*, 79−88.
(13) Aramburo, L. R.; Ruiz-Martínez, J.; Sommer, L.; Arstad, B.; Buitrago-Sierra, R.; Sepúlveda-Escribano, A.; Zandbergen, H. W.; Olsbye, U.; de Groot, F. M. F.; Weckhuysen, B. M. X-Ray Imaging of SAPO-34 Molecular Sieves at the Nanoscale: Influence of Steaming on the Methanol-to-Hydrocarbons Reaction. *ChemCatChem* **2013**, *5*, 1386−1394.
(14) Sastre, G.; Lewis, D. W.; Catlow, C. R. A. Mechanisms of silicon incorporation in aluminophosphate molecular sieves. *J. Mol. Catal. A: Chem.* **1997**, *119*, 349−356.
(15) Olsbye, U.; Svelle, S.; Bjørgen, M.; Beato, P.; Janssens, T. V. W.; Joensen, F.; Bordiga, S.; Lillerud, K. P. Conversion of Methanol to Hydrocarbons: How Zeolite Cavity and Pore Size Controls Product Selectivity. *Angew. Chem., Int. Ed.* **2012**, *51*, 5810−5831.
(16) Briend, M.; Shikholeslami, A.; Peltre, M.-J.; Delafosse, D.; Barthomeuf, D. Thermal and hydrothermal stability of SAPO-5 and SAPO-37 molecular sieves. *J. Chem. Soc., Dalton Trans.* **1989**, 1361−1362.
(17) Corma, A.; Fornés, V.; Franco, M. J.; Mocholí, F. A.; Pérez-Pariente, J. Hydrothermal Stability and Cracking Behavior of Silicoaluminophosphate Molecular Sieve-37 with Different Silicon Contents. In *Fluid Catalytic Cracking II,* Occelli, M. L., Ed. American Chemical Society: Washington DC, 1991; Vol. *452*, pp 79−95.
(18) Buchholz, A.; Wang, W.; Arnold, A.; Xu, M.; Hunger, M. Successive steps of hydration and dehydration of silicoaluminophosphates H-SAPO-34 and H-SAPO-37 investigated by in situ CF MAS NMR spectroscopy. *Microporous Mesoporous Mater.* **2003**, *57*, 157−168.
(19) Sieverts, A. Information on the occlusion and diffusion of gases through metals. *Z. Phys. Chem.* **1907**, *60*, 129−201.
(20) Broom, D. P. The accuracy of hydrogen sorption measurements on potential storage materials. *Int. J. Hydrogen Energy* **2007**, *32*, 4871−4888.
(21) Arstad, B.; Lind, A.; Cavka, J. H.; Thorshaug, K.; Akporiaye, D.; Wragg, D.; Fjellvåg, H.; Grønvold, A.; Fuglerud, T. Structural changes in SAPO-34 due to hydrothermal treatment. A NMR, XRD, and DRIFTS study. *Microporous Mesoporous Mater.* **2016**, *225*, 421−431.
(22) Kalantzopoulos, G. N.; Lundvall, F.; Checchia, S.; Lind, A.; Wragg, D. S.; Fjellvåg, H.; Arstad, B. In situ flow MAS NMR spectroscopy and synchrotron PDF analyses of the local response of the Brønsted acidic site in SAPO-34 during hydration at elevated temperatures. *ChemPhysChem* **2018**, *19*, 519−528.
(23) Sławiński, W. A.; Wragg, D. S.; Akporiaye, D.; Fjellvåg, H. Intergrowth structure modelling in silicoaluminophosphate SAPO-18/34 family. *Microporous Mesoporous Mater.* **2014**, *195*, 311−318.
(24) Franco, M. J.; Pérez-Pariente, J.; Misud, A.; Blasco, T.; Sanz, J. Crystallization kinetics of SAPO-37. *Zeolites* **1992**, *12*, 386−394.
(25) Dyadkin, V.; Pattison, P.; Dmitriev, V.; Chernyshov, D. A new multipurpose diffractometer PILATUS@SNBL. *J. Synchrotron Radiat.* **2016**, *23*, 825−829.
(26) Fjermestad, T.; Svelle, S.; Swang, O. Mechanistic Comparison of the Dealumination in SSZ-13 and the Desilication in SAPO-34. *J. Phys. Chem. C* **2013**, *117*, 13442−13451.
(27) Stinton, G. W.; Evans, J. S. O. Parametric Rietveld refinement. *J. Appl. Crystallogr.* **2007**, *40*, 87−95.
(28) *TOPAS 5.0, Bruker AXS*. Available from: http://www.topas-academic.net/ (Accessed: Dec 15, 2019).
(29) Brandenburg, K. *Diamond, 3.2k*; Crystal Impact GbR: Bonn, German, 2014.
(30) Momma, K.; Izumi, F. VESTA 3 for three-dimensional visualization of crystal, volumetric and morphology data. *J. Appl. Crystallogr.* **2011**, *44*, 1272−1276.
(31) Shearer, G. C.; Chavan, S.; Bordiga, S.; Svelle, S.; Olsbye, U.; Lillerud, K. P. Defect Engineering: Tuning the Porosity and Composition of the Metal−Organic Framework UiO-66 via Modulated Synthesis. *Chem. Mater.* **2016**, *28*, 3749−3761.
(32) Antoniou, M. K.; Diamanti, E. K.; Enotiadis, A.; Policicchio, A.; Dimos, K.; Ciuchi, F.; Maccallini, E.; Gournis, D.; Agostino, R. G. Methane storage in zeolite-like carbon materials. *Microporous Mesoporous Mater.* **2014**, *188*, 16−22.
(33) Antoniou, M. K.; Policicchio, A.; Dimos, K.; Gournis, D.; Karakassides, M. A.; Agostino, R. G. Naphthalene-based periodic nanoporous organosilicas: II. Hydrogen and methane adsorption and physicochemical study. *Microporous Mesoporous Mater.* **2012**, *158*, 332−338.
(34) Kalantzopoulos, G. N.; Policicchio, A.; Maccallini, E.; Krkljus, I.; Ciuchi, F.; Hirscher, M.; Agostino, R. G.; Golemme, G. Resistance to the transport of H-2 through the external surface of as-made and modified silicalite-1 (MFI). *Microporous Mesoporous Mater.* **2016**, *220*, 290−297.
(35) Kalantzopoulos, G. N.; Antoniou, M. K.; Enotiadis, A.; Dimos, K.; Maccallini, E.; Policicchio, A.; Colavita, E.; Agostino, R. G. Enhanced hydrogen and methane storage of hybrid mesoporous organosilicas. *J. Mater. Chem. A* **2016**, *4*, 9275−9285.
(36) Kalantzopoulos, G. N.; Enotiadis, A.; Maccallini, E.; Antoniou, M.; Dimos, K.; Policicchio, A.; Klontzas, E.; Tylianakis, E.; Binas, V.; Trikalitis, P. N.; Agostino, R. G.; Gournis, D.; Froudakis, G. E. Hydrogen storage in ordered and disordered phenylene-bridged mesoporous organosilicas. *Int. J. Hydrogen Energy* **2014**, *39*, 2104−2114.
(37) Foster, M. D.; Rivin, I.; Treacy, M. M. J.; Delgado Friedrichs, O. A geometric solution to the largest-free-sphere problem in zeolite frameworks. *Microporous Mesoporous Mater.* **2006**, *90*, 32−38.
(38) Tóth, J. Uniform Interpretation of Gas/Solid Adsorption. *Adv. Colloid Interface Sci.* **1995**, *55*, 1−239.
(39) Steiner, T. The Hydrogen Bond in the Solid State. *Angew. Chem., Int. Ed.* **2002**, *41*, 48−76.
(40) Zhang, L.; Chen, K.; Chen, B.; White, J. L.; Resasco, D. E. Factors that Determine Zeolite Stability in Hot Liquid Water. *J. Am. Chem. Soc.* **2015**, *137*, 11810−11819.
(41) Agostini, G.; Lamberti, C.; Palin, L.; Milanesio, M.; Danilina, N.; Xu, B.; Janousch, M.; van Bokhoven, J. A. In Situ XAS and XRPD Parametric Rietveld Refinement To Understand Dealumination of Y Zeolite Catalyst. *J. Am. Chem. Soc.* **2010**, *132*, 667−678.
(42) Ravenelle, R. M.; Schüβler, F.; D'Amico, A.; Danilina, N.; van Bokhoven, J. A.; Lercher, J. A.; Jones, C. W.; Sievers, C. Stability of Zeolites in Hot Liquid Water. *J. Phys. Chem. C* **2010**, *114*, 19582−19595.
(43) Heard, C. J.; Grajciar, L.; Rice, C. M.; Pugh, S. M.; Nachtigall, P.; Ashbrook, S. E.; Morris, R. E. Fast room temperature lability of aluminosilicate zeolites. *Nat. Commun.* **2019**, *10*, 4690.
(44) Yamanaka, N.; Itakura, M.; Kiyozumi, Y.; Ide, Y.; Sadakane, M.; Sano, T. Acid stability evaluation of CHA-type zeolites synthesized by interzeolite conversion of FAU-type zeolite and their membrane application for dehydration of acetic acid aqueous solution. *Microporous Mesoporous Mater.* **2012**, *158*, 141−147.
(45) Kletnieks, P. W.; Ehresmann, J. O.; Nicholas, J. B.; Haw, J. F. Adsorbate Clustering and Proton Transfer in Zeolites: NMR Spectroscopy and Theory. *ChemPhysChem* **2006**, *7*, 114−116.

https://dx.doi.org/10.1021/acs.chemmater.9b04510
Chem. Mater. 2020, 32, 1495−1505

(46) Vjunov, A.; Wang, M.; Govind, N.; Huthwelker, T.; Shi, H.; Mei, D.; Fulton, J. L.; Lercher, J. A. Tracking the Chemical Transformations at the Brønsted Acid Site upon Water-Induced Deprotonation in a Zeolite Pore. *Chem. Mater.* **2017**, *29*, 9030−9042.
(47) Arstad, B.; Kolboe, S. Methanol-to-hydrocarbons reaction over SAPO-34. Molecules confined in the catalyst cavities at short time on stream. *Catal. Lett.* **2001**, *71*, 209−212.

https://dx.doi.org/10.1021/acs.chemmater.9b04510
Chem. Mater. 2020, 32, 1495−1505